Vacancy-Stabilized Superionic State in Na$_{3-x}$Sb$_{1-x}$W$_x$S$_4$

Shin-ichi Nishimura,[†,‡] Akitoshi Hayashi,[¶,‡] Atsushi Sakuda,[¶] and Atsuo Yamada[*,†,‡]

†Department of Chemical System Engineering, Graduate School of Engineering, The University of Tokyo, 7-3-1 Hongo, Bunkyo-ku, Tokyo 113-8656, Japan

‡Elements Strategy Initiative for Catalysts & Batteries (ESICB), Kyoto University, Katsura, Nishikyo-ku, Kyoto 615-8245, Japan

¶Department of Applied Chemistry, Graduate School of Engineering, Osaka Prefecture University, 1-1 Gakuen-cho, Sakai, Osaka, Japan

ABSTRACT: The discovery of numerous superionic conductors has accelerated the development of solid-state energy storage systems. Among all alkaline-ionic conductors known thus far, Na$_{3-x}$Sb$_{1-x}$W$_x$S$_4$ exhibits the highest ionic conductivity of > 30 mS cm^{-1} at ambient temperature, even surpassing the conductivity of the best lithium superionic conductor. The origin of the peculiar high Na$^+$ diffusivity was investigated by the in-depth crystallographic analysis of Na$_{3-x}$Sb$_{1-x}$W$_x$S$_4$ through combined X-ray diffraction and molecular dynamics simulations, emphasizing the accurate three-dimensional disordered nature of sodium in the crystalline matrix. The important features induced by the aliovalent tungsten substitution were (i) tetragonal to cubic transformation, (ii) the creation of sodium vacancies that are evenly distributed throughout the crystal without the local condensation around W, and (iii) the effective formation of sodium positional disordering by sodium vacancy. These features inherent to the best alkaline-ion conducting phase reported thus far would provide invaluable insights toward the further development of superionic conductors.

Solid sodium-ion conductors have been studied as an important component of electrochemical energy storage devices. For example, sodium-β-alumina is a vital electrolyte material in sodium-sulfur batteries that operate at elevated temperatures of approximately 600 K.[1] An electrolyte for battery applications requires a high ionic conductivity to offer a high energy efficiency and power at the operating temperature. Continuous efforts for the development of sodium-ion conductors have led to materials with extremely high conductivities comparable to those of liquid electrolytes and have stimulated the development of all-solid-state sodium batteries. Hayashi *et al.*, have recently discovered the emergent sodium superionic phase, Na$_{3-x}$Sb$_{1-x}$W$_x$S$_4$, which exhibits an ionic conductivity > 30 mS cm^{-1} at 298 K.[2] This outstanding ionic conductivity is the highest among those reported for solid sodium-ion conductors thus far, and even higher than those of the sophisticated lithium superionic conductors.[2,3] Considering the smaller surface charge densities and the larger polarizabilities of sodium ions compared to those of lithium ions, sodium-ion conductors that largely outperform the lithium-ion conductors would be worth exploring.

At the initial stages of research related to sodium-ion conductors, various oxide-based conductors have been studied. However, the recent focus has been shifted to sulfide-based materials, mainly thioanionic compounds with high conductivities. Initiated by the identification of Na$_3$PS$_4$ glass ceramics with a conductivity of > 0.1 mS cm^{-1} at 300 K[4] a number of sulfide/selenide-based sodium-ion conductors—including thioanions and selenoanions—have been reported, for e.g., Na$_3$PS$_4$,[4] Na$_3$PSe$_4$,[5] Na$_3$SbSe$_4$,[6] Na$_{10}$SnP$_2$S$_{12}$,[7] Na$_{11}$Sn$_2$PS$_{12}$,[8] and Na$_{10}$GeP$_2$S$_{12}$[9]. Among these, Na$_3$SbS$_4$ exhibits a prominent chemical stability.[10–12] Although most of the thioanionic sodium and lithium compounds are prone to react with water and produce highly toxic hydrogen sulfide, Na$_3$SbS$_4$ can be protected by the self-formation of a stable hydrated phase that prohibits the generation of hydrogen sulfide.

The superionic phase, Na$_{3-x}$Sb$_{1-x}$W$_x$S$_4$, which was recently discovered by Hayashi *et al.*,[2] can be considered as a solid solution in the Na$_3$SbS$_4$–Na$_2$WS$_4$ system. The aliovalent tungsten(VI) substitution to antimony(V) and the simultaneous introduction of sodium vacancy significantly increases the ionic conductivity from 1 mS cm^{-1} to > 30 mS cm^{-1}.[2] The preliminary structural analysis presented in the original research suggests that it crystallizes into the β-Na$_3$PS$_4$-type structure with the aforementioned sodium vacancies.[2] However, the quantitative confirmation of the structural model with anharmonic ion distributions has not yet been achieved.
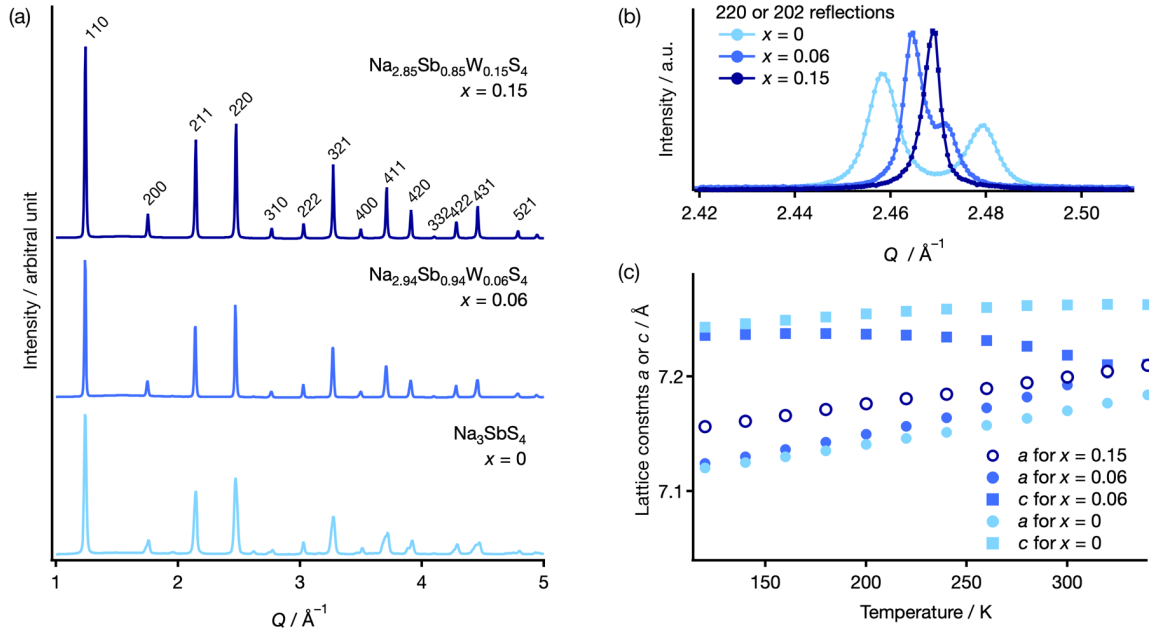
Figure 1 (a) Powder X-ray diffraction patterns of $Na_{3-x}Sb_{1-x}W_xS_4$ (x = 0, 0.06, and 0.15) at RT. (b) Peak profiles of 220 and 202 Bragg reflections collected by a high-angular-resolution diffractometer at RT. (c) Lattice constants measured at temperatures ranging from 120–340 K.

In this study, the origin of the peculiar Na^+ mobility in $Na_{3-x}Sb_{1-x}W_xS_4$ was investigated via in-depth crystallographic analysis by combining the X-ray diffraction and molecular dynamics (MD) simulations, revealing the accurate three-dimensional (3D) disordered nature of sodium in the crystalline matrix. In addition to the overall trend in which the aliovalent tungsten substitution stabilizes the room-temperature superionic cubic phase isostructural to the β-Na_3PS_4, the distribution of sodium vacancies and its vital role in sodium conduction are highlighted in the following sections.

Figure 1 (a) shows the powder X-ray diffraction patterns of $Na_{3-x}Sb_{1-x}W_xS_4$ measured for x = 0, 0.06, and 0.15 at RT. In general, the partial aliovalent tungsten (VI) substitution stabilizes the cubic β-Na_3PS_4-type structure (commonly observed as the high-temperature phase), $cI16$ in the Pearson symbol code, even at RT. For the non-substituted sample, the Bragg reflections are indexed with a tetragonal lattice— which is consistent with previous reports as described in the Pearson symbol code $tP16$ and is isostructural to α-Na_3PS_4 with $P\bar{4}2_1c$ symmetry, which is commonly observed as the low-temperature phase. For the intermediate W-substituted sample (x = 0.06), the tetragonal distortion of the crystal lattice is less obvious, approaching the cubic β-Na_3PS_4 phase. For x = 0.15, all the observed Bragg reflections can be indexed with a body-centered cubic lattice, where no tetragonal distortion is distinguishable even by high-angular-resolution measurements (Figure 1(b)). The remaining tetragonal distortion at x = 0.06, evidenced in the splitting of Bragg reflections in Figure 1(b), becomes more pronounced at low temperatures, while it vanishes at a temperature slightly above the ambient temperature. Figure 1(c) demonstrates the plot of the lattice constants of $Na_{3-x}Sb_{1-x}W_xS_4$ evaluated at temperatures ranging from 120 K to 340 K. For x = 0.06, the lattice distortion was distinguishable up to

320 K and became negligible at 340 K. For x = 0 and 0.15, no tetragonal-cubic transitions existed at this temperature range.

Based on the phase relationships, we performed structural refinements with the tetragonal α-Na_3PS_4 model for x = 0 and 0.06 and the cubic β-Na_3PS_4 model for x = 0.15. The calculated diffraction patterns were consistent with those observed experimentally. (See Supporting Information, Figure S1). The crystallographic information can be found in Supporting Information Table S1.

Figure 2 shows the refined structure model of $Na_{2.85}Sb_{0.85}W_{0.15}S_4$ (x = 0.15) and sodium probability density distributions. The cubic phase of x = 0.15 demonstrates a characteristic sodium density distribution similar to that of
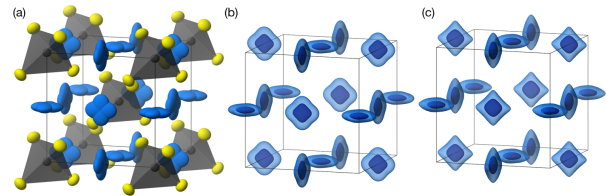

Figure 2 Crystal structure model and Na density distribution of $Na_{2.85}Sb_{0.85}W_{0.15}S_4$ (x = 0.15) at 300 K. (a) Structure model represented with thermal ellipsoids in 80% probability. Blue, gray, and yellow ellipsoids represent sodium, antimony/tungsten, and sulfur atoms, respectively. (b) Isosurfaces of probability density distribution for Na derived from the refined structural parameters of Na in the Rietveld refinement. Dark and light color surfaces show 1 and 0.1 Å^{-3} levels, respectively. (c) Same as (b) but derived from the DFT-MD trajectory of $Na_{2.875}Sb_{0.875}W_{0.125}S_4$ (x = 0.125) at 300 K.

2

β-Na$_3$PS$_4$. Locating the sodium at the center of the average position (6b site) with the harmonic thermal vibration failed to satisfactorily reproduce the experimental diffraction intensity. Therefore, we adopted a split-site model as applied to β-Na$_3$PS$_4$ to represent the strong anharmonicity and anisotropy of the sodium density distribution. The split-site model reduced the agreement factor of Bragg intensities R_B[1] from 3.70% to 1.47% and flattened the difference Fourier map about the sodium site. The strong anharmonicity and anisotropy of sodium in Na$_{3-x}$Sb$_{1-x}$W$_x$S$_4$ reflects the dynamic sodium distribution, which is consistent with the high ionic conductivity at room temperature. A similar dynamic behavior in β-Na$_3$PS$_4$ is preserved at temperatures > 530 K.[13–15]

For more detailed and multi-angle analyses of sodium distribution, we conducted density functional theory (DFT)-based MD simulations for Na$_{2.875}$Sb$_{0.875}$W$_{0.125}$S$_4$. Figure 2(c) represents the obtained probability density distributions of sodium at 300 K, which are similar to those reported by Jalem et al.[16] The experimental sodium distribution constructed using the data from the diffraction analysis are well reproduced, where the sodium site in Na$_{2.85}$Sb$_{0.85}$W$_{0.15}$S$_4$ shows strong anharmonicity—reflecting the high tolerance to the local displacement of Na$^+$. The dynamic and non-periodic nature of the ion displacement should promote the local ionic mobility, while in α-Na$_3$PS$_4$, the sodium displacements are more static and crystallized, rendering them less mobile.[15,17]
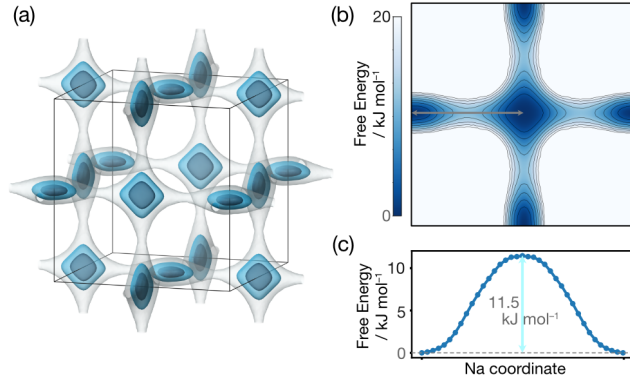

Figure 3 Free energy landscape of sodium in Na$_{2.875}$ Sb$_{0.875}$ W$_{0.125}$ S$_4$ at 300 K derived from DFT-MD trajectory. (a) Three-dimensional representation with isosurface levels at 13, 6, and 2 kJ mol^{-1} in gray, light-blue, and blue colors, respectively. (b) Color-scaled two-dimensional map on (100) plane at x = 0. Contours are drawn at 2.5–20 kJ mol^{-1} with intervals of 2.5 kJ mol^{-1}. (c) One-dimensional profile along a minimum free energy pathway for sodium migration (along the gray arrow in (b)).

To discuss the global ionic mobility, we derived the free energy of sodium, F from the probability density of sodium ρ as follows:

$$F = -k_\mathrm{B}T\log\frac{\rho}{\rho_0}$$

where ρ_0 is the sodium probability density at the center of the site, and k_B is the Boltzmann constant. Figure 3 shows the free energy landscape of sodium calculated from the DFT-MD trajectories for Na$_{2.875}$Sb$_{0.875}$W$_{0.125}$S$_4$ at 300 K. The minimum energy pathway for sodium migration is along the linear lines connecting each sodium average site (6b sites of $I\bar{4}3m$), where the free energy barrier for migration is very small, 11.5 kJ mol^{-1} (119 meV). Such a low energy barrier is indicative of an excellent measured sodium conductivity, which is higher than 30 mS cm^{-1} even at room temperature, as well as a low activation energy (< 20 kJ mol^{-1}). In a general sense, the origin of the low-energy barrier could be a large bottleneck in the structure. However, the Na–S interatomic distance at the bottleneck position is 2.675(4) Å, which is shorter than that of the β-Na$_3$PS$_4$, 2.6966(5) Å.[15] While Na$_{3-x}$Sb$_{1-x}$W$_x$S$_4$ has a larger lattice volume and larger thioanion than β-Na$_3$PS$_4$, the bottleneck size is smaller. Therefore, other factors may be crucial in explaining the low migration barrier for the inter-site sodium motion.
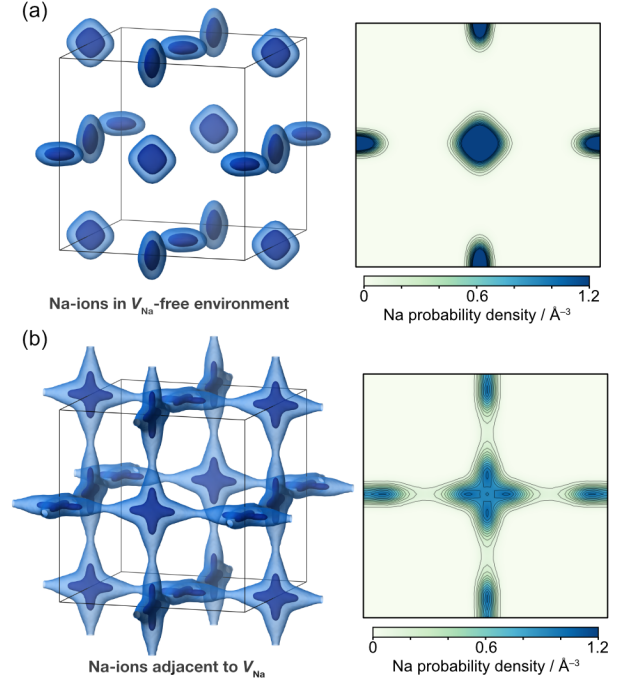

Figure 4 Partial probability density distributions of sodium distinguished by the presence of sodium vacancy v'_{Na} at the nearest neighbor sites. (a) Free from the sodium vacancy. (b) Adjacent to the sodium vacancy v'_{Na}. Left panels show 3D representations with isosurfaces at 1 and 0.1 Å^{-3} levels, colored with light blue and blue, respectively. Right panels show color-scaled maps on (100) plane at x = 0 with contours at levels of 0.08–1.2 Å^{-3} with 0.08 intervals. Probability density was normalized by the number of sodium atoms in the unit cell.

---

1 $R_B = \frac{\sum_{hkl}|I_{\mathrm{obs},hkl} - I_{\mathrm{calc},hkl}|}{\sum_{hkl}I_{\mathrm{obs},hkl}}$, $I_{\mathrm{obs},hkl}$: the observed intensity of hkl Bragg reflection and $I_{\mathrm{calc},hkl}$: the calculated intensity of hkl Bragg reflection.

To explain the peculiar sodium diffusivity from another viewpoint, we analyzed the sodium vacancy effects enhancing the sodium mobility. For the disentanglement of sodium dynamics and its correlation with the vacancies introduced, from the DFT-MD results, a more detailed analysis of the sodium density distribution was conducted. We defined two types of sodium atoms: vacancy-related and vacancy-free Na. Vacancy-related Na is defined as a sodium adjacent to vacant sodium sites. The remaining Na atoms correspond to the vacancy-free Na. In the present simulation, 2 of the 48 sites are vacant, and 8 or 6 of the 46 sodium atoms are classified as vacancy-related sodium atoms at each MD time step. As shown in Figure 4(a), the vacancy-free sodium shows a localized character, while the vacancy-related sodium shows a diffuse distribution spreading toward the adjacent sites, where a significant probability is distinguishable even at the bottleneck position (Figure 4(b)). The sodium vacancy induces displacements of the neighboring sodium ions from the average position, and makes inter-site jumps possible.

To clarify the role of the W substitution, we calculated the sodium distribution around the substituted tungsten from the trajectories of the DFT-MD simulations. The substitution of Sb(V) with W(VI) creates a positive-charge point to induce adjacent sodium vacancies. Therefore, classical/intuitive coulombic considerations might lead us to expect the sodium vacancy condensation around such a positive charge (W sites). However, the average sodium occupancies were close to the global average at the first, second, and third nearest neighbor sites (Table S2 in Supporting Information). Thus, the vacancy condensation around the substitution site was not significant. Moreover, the majority of the sodium ions around the W sites are highly mobile. Figure 5 shows the average probability density of sodium around the substituted site, which forms the tetrathiotungstate anion $[WS_4]^{2-}$. In the 3D Na distribution around the W site, all the Na^+ sites exhibited a diffuse spatial distribution spreading toward the neighboring outer sites, while the first nearest neighbor Na^+ showed a relatively localized character. These statistical characteristics indicate that the W substitution introduces globally distributed sodium vacancies, each of which effectively create Na with positional disordering. Hence, the vacancy-induced sodium dynamics were not constrained to the substituted site.
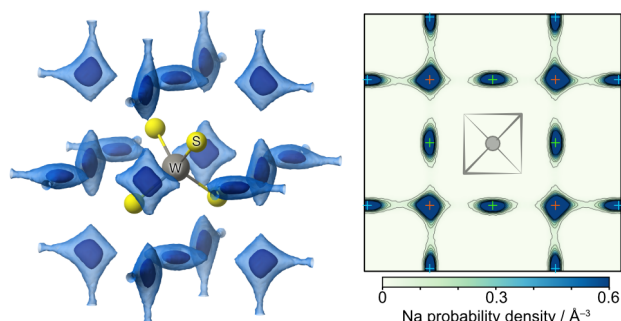

Figure 5 Probability density distribution of sodium around the tetrathiotungstate anion $[WS_4]^{2-}$. Left panel is a 3D representation with light blue and blue isosurfaces at 0.1 and 1 Å^{-3}, respectively. Sulfur and tungsten atoms are represented in yellow and gray spheres, respectively. Right panel is a color-scaled map sliced at (100) plane with contours at 0.04–0.6 Å^{-3}. Green, red,

and blue crosses indicate the first, second, and third nearest neighbor sites.

In summary, we have demonstrated the crystal structure of the sodium superionic phase $Na_{3-x}Sb_{1-x}W_xS_4$, including details on sodium dynamics. The cubic β-Na_3PS_4-type structure is stabilized by the substitution of W(VI) with Sb(V) and the introduction of sodium vacancies. The dynamic probability density distribution analyses confirmed that the sodium vacancies did not localize around the substituted W site, and the globally distributed sodium vacancies effectively disordered the adjacent sodium ions to realize an extremely high alkaline-ion conductivity, which is the highest reported thus far. The material design in this system and the aliovalent substitution to the Sb(V) site is an archetypal strategy and might be one of the most ideal ways to realize the sodium superionic phase.

ASSOCIATED CONTENT

Supporting Information

The Supporting Information is available free of charge on the ACS Publications website.
Methods and profile refinement results of powder diffraction data. (PDF)
Crystal structure information (CIF)

AUTHOR INFORMATION

Corresponding Author

* Atsuo Yamada – Department of Chemical System Engineering, Graduate School of Engineering, The University of Tokyo, 7-3-1 Hongo, Bunkyo-ku, Tokyo 113-8656, Japan; Email: yamada@chemsys.t.u-tokyo.ac.jp

ABBREVIATIONS

RT, room temperature; 3D, three-dimensional; DFT, density functional theory; MD, molecular dynamics.

REFERENCES

(1)   Oshima, T.; Kajita, M.; Okuno, A. Development of Sodium-Sulfur Batteries. *International Journal of Applied Ceramic Technology* **2004**, *1* (3), 269–276. https://doi.org/https://doi.org/10.1111/j.1744-7402.2004.tb00179.x.

(2)   Hayashi, A.; Masuzawa, N.; Yubuchi, S.; Tsuji, F.; Hotehama, C.; Sakuda, A.; Tatsumisago, M. A Sodium-Ion Sulfide Solid Electrolyte with Unprecedented

Conductivity at Room Temperature. *Nature Communications* **2019**, *10* (1), 5266. https://doi.org/10.1038/s41467-019-13178-2.

(3) Kato, Y.; Hori, S.; Saito, T.; Suzuki, K.; Hirayama, M.; Mitsui, A.; Yonemura, M.; Iba, H.; Kanno, R. High-Power All-Solid-State Batteries Using Sulfide Superionic Conductors. *Nature Energy* **2016**, *1* (4), 16030. https://doi.org/10.1038/nenergy.2016.30.

(4) Hayashi, A.; Noi, K.; Sakuda, A.; Tatsumisago, M. Superionic Glass-Ceramic Electrolytes for Room-Temperature Rechargeable Sodium Batteries. *Nat. Commun.* **2012**, *3*, 856.

(5) Zhang, L.; Yang, K.; Mi, J.; Lu, L.; Zhao, L.; Wang, L.; Li, Y.; Zeng, H. Na3PSe4: A Novel Chalcogenide Solid Electrolyte with High Ionic Conductivity. *Advanced Energy Materials* **2015**, *5* (24), 1501294. https://doi.org/https://doi.org/10.1002/aenm.201501294.

(6) Xiong, S.; Liu, Z.; Rong, H.; Wang, H.; McDaniel, M.; Chen, H. Na3SbSe4–xSxas Sodium Superionic Conductors. *Scientific Reports* **2018**, *8* (1), 9146. https://doi.org/10.1038/s41598-018-27301-8.

(7) Richards, W. D.; Tsujimura, T.; Miara, L. J.; Wang, Y.; Kim, J. C.; Ong, S. P.; Uechi, I.; Suzuki, N.; Ceder, G. Design and Synthesis of the Superionic Conductor Na10SnP2S12. *Nat. Commun.* **2016**, *7*. https://doi.org/10.1038/ncomms11009.

(8) Zhang, Z.; Ramos, E.; Lalère, F.; Assoud, A.; Kaup, K.; Hartman, P.; Nazar, L. F. Na11Sn2PS12: A New Solid State Sodium Superionic Conductor. *Energy & Environmental Science* **2018**, *11* (1), 87–93. https://doi.org/10.1039/C7EE03083E.

(9) Tsuji, F.; Tanibata, N.; Sakuda, A.; Hayashi, A.; Tatsumisago, M. Preparation of Sodium Ion Conductive Na10GeP2S12 Glass-Ceramic Electrolytes. *Chemistry Letters* **2017**, *47* (1), 13–15. https://doi.org/10.1246/cl.170836.

(10) Wang, H.; Chen, Y.; Hood, Z. D.; Sahu, G.; Pandian, A. S.; Keum, J. K.; An, K.; Liang, C. An Air-Stable Na3SbS4 Superionic Conductor Prepared by a Rapid and Economic Synthetic Procedure. *Angewandte Chemie International Edition* **2016**, *55* (30), 8551–8555. https://doi.org/https://doi.org/10.1002/anie.201601546.

(11) Banerjee, A.; Park, K. H.; Heo, J. W.; Nam, Y. J.; Moon, C. K.; Oh, S. M.; Hong, S.-T.; Jung, Y. S. Na3SbS4: A Solution Processable Sodium Superionic Conductor for All-Solid-State Sodium-Ion Batteries. *Angewandte Chemie International Edition* **2016**, *55* (33), 9634–9638. https://doi.org/https://doi.org/10.1002/anie.201604158.

(12) Zhang, L.; Zhang, D.; Yang, K.; Yan, X.; Wang, L.; Mi, J.; Xu, B.; Li, Y. Vacancy-Contained Tetragonal Na3SbS4 Superionic Conductor. *Advanced Science* **2016**, *3* (10), 1600089. https://doi.org/https://doi.org/10.1002/advs.201600089.

(13) Blachnik, R.; Rabe, U. Das Thermische Verhalten Der Mischungen Na2S–P4S10 Und Na4Ge4S10–P4S10 Des Systems Na2S–GeS2–P4S10. *Zeitschrift für anorganische und allgemeine Chemie* **1980**, *462* (1), 199–206. https://doi.org/https://doi.org/10.1002/zaac.19804620122.

(14) Jansen, M.; Henseler, U. Synthesis, Structure Determination, and Ionic Conductivity of Sodium Tetrathiophosphate. *J. Solid State Chem.* **1992**, *99* (1), 110–119. https://doi.org/http://dx.doi.org/10.1016/0022-4596(92)90295-7.

(15) Nishimura, S.; Tanibata, N.; Hayashi, A.; Tatsumisago, M.; Yamada, A. The Crystal Structure and Sodium Disorder of High-Temperature Polymorph β-Na3PS4. *Journal of Materials Chemistry A* **2017**, *5* (47), 25025–25030. https://doi.org/10.1039/C7TA08391B.

(16) Jalem, R.; Hayashi, A.; Tsuji, F.; Sakuda, A.; Tateyama, Y. First-Principles Calculation Study of Na+ Superionic Conduction Mechanism in W- and Mo-Doped Na3SbS4 Solid Electrolytes. *Chemistry of Materials* **2020**, *32* (19), 8373–8381. https://doi.org/10.1021/acs.chemmater.0c02318.

(17) Yu, C.; Ganapathy, S.; de Klerk, N. J. J.; van Eck, E. R. H.; Wagemaker, M. Na-Ion Dynamics in Tetragonal and Cubic Na3PS4, a Na-Ion Conductor for Solid State Na-Ion Batteries. *Journal of Materials Chemistry A* **2016**, *4* (39), 15095–15105. https://doi.org/10.1039/C6TA05896E.

(18) Momma, K.; Izumi, F. VESTA3 for Three-Dimensional Visualization of Crystal, Volumetric and Morphology Data. *J. Appl. Cryst.* **2011**, *44* (6), 1272–1276. https://doi.org/10.1107/S0021889811038970.

Insert Table of Contents artwork here

v_{Na}-free

Adjacent to v_{Na}